Statistically equivalent surrogate material models: Impact of random imperfections on the elasto-plastic response

Ustim Khristenko, Andrei Constantinescu, Patrick Le Tallec, Barbara Wohlmuth

Statistically equivalent surrogate material models and the impact of random imperfections on elasto-plastic response

Ustim Khristenko[a,*], Andrei Constantinescu[b], Patrick Le Tallec[b], Barbara Wohlmuth[a]

[a] *Department of Mathematics, Technical University of Munich, Garching, Germany*
[b] *Laboratoire de Mécanique des Solides, CNRS - École Polytechnique - Institut Polytechnique de Paris, Palaiseau, France*

Abstract

Manufactured materials usually contain random imperfections due to the fabrication process, e.g., the 3D-printing, casting, etc. These imperfections affect significantly the effective material properties and result in uncertainties in the mechanical response. Numerical analysis of the effects of the imperfections and the uncertainty quantification (UQ) can be often done by use of digital stochastic surrogate material models. In this work, we present a new flexible class of surrogate models depending on a small number of parameters with special focus on two-phase materials. The surrogate models are constructed as the level-set of a linear combination of an intensity field representing the topological shape and a Gaussian perturbation representing the imperfections. The mathematical design parameters of the model are related to physical ones and thus easy to interpret. The calibration of the model parameters is performed using progressive batching sub-sampled quasi-Newton minimization, using a designed distance measure between the synthetic samples and the data. Then, employing a fast sampling algorithm, an arbitrary number of synthetic samples can be generated to use in Monte Carlo type methods. In particular, we illustrate the method in application to UQ of the elasto-plastic response of an imperfect octet-truss lattice which plays an important role in additive manufacturing. To this end, we study the effective material properties of the lattice unit cell under elasto-plastic deformations and investigate the sensitivity of the effective Young's modulus to the imperfections.

Keywords: additive manufacturing, surrogate model, random fields, stochastic optimization, uncertainty quantification, elasto-plastic material

Dedication: The authors would like to express their deepest gratitude to Dr. J. Tinsley Oden. We admire him as a great scientist with unique and exceptional contributions in many areas, as a kind and gentle person, as a dedicated teacher who has influenced many of us in our career and scientific life, and as a person to whom we are deeply attached and thankful. Without him, the paper would never have been started and would never have been completed. Throughout the project, he was a reliable source of inspiration, advice and encouragement. We want to dedicate this paper to him.

1. Introduction

In structural design, the shape and architecture of manufactured materials are usually optimized assuming perfect, defect-free geometries. However, the as-manufactured material may differ from the as-designed one, in particular, owing to defects and imperfections induced by the manufacturing process. Typical examples are the structures manufactured using 3D-printing technologies. Moreover, the process-induced imperfections may significantly affect the effective properties of the manufactured material with respect to the as-designed structure [43, 55, 65, 23, 33]. In this framework, more robust material design requires to take the imperfections into account during topology optimization. A general pipeline for such imperfections-aware

*Corresponding author
Email addresses: khristen@ma.tum.de (Ustim Khristenko), andrei.constantinescu@polytechnique.edu (Andrei Constantinescu), patrick.letallec@polytechnique.edu (Patrick Le Tallec), wohlmuth@ma.tum.de (Barbara Wohlmuth)

topology optimization was proposed in [51]. Since the imperfections are random in nature, the characterization of the properties of manufactured materials is performed using statistical methods. Therefore, given that the number of real as-manufactured samples is limited, a common strategy is to develop a so-called *digital twin* – a mathematical model of a surrogate material given by a random field reproducing the topological shape and imitating statistical properties of the target real-world material. The philosophy is to introduce a flexible class of surrogate materials characterized by several design parameters that need to be tuned. Then, a numerical model can be employed using methods of *uncertainty quantification* (UQ), wherein the statistics of physical models with uncertainties is accounted for, and in which random fields typically enter as simulation inputs.

The use of modern machine learning (ML) methods has become a popular and powerful approach for the construction of surrogate models; see, e.g., [12, 24, 22, 19]. However, ML is often used as a closed black box tool, in which the created model may depend on a large number of non-interpretable parameters, and requires a large amount of training data. In order to simplify such approaches, we focus on cases in which the topological shape of the structure is known a priori, and the uncertainties include only the process-induced imperfections. In this situation, only a few geometrically interpretable parameters are sufficient to describe the model.

In this work, we represent the material as a random phase field. Considering a class of surrogate material models characterized by several *design* parameters, we look for a projection of the target material onto this class by minimizing the distance between vectors of statistical descriptors associated with surrogate samples and the data, respectively.

We discuss a unified form of surrogate models for two-phase heterogeneous materials which present deterministic topological shapes but are subject to uncertain imperfections. We formulate the surrogate phase field via the level-set method; see, e.g, [5, 6, 72, 4, 52, 34]. The introduced level-set function (called the intensity) is a random field given by a combination of the known topological structure and a random perturbation field representing the imperfections. Several given examples reproducing particular two-phase structure types such as pores, beams, cracks, lattices, etc., illustrate the flexibility of the proposed surrogate model class.

We then apply the proposed model for a 3D-printed octet-truss lattice, which is a popular architecture in additive manufacturing [68, 57, 9]. First, we calibrate the model such that it reproduces statistical properties of several manufactured material samples obtained from X-ray computed tomography (CT) measurements. To this end, we formulate and solve a stochastic optimization problem to identify the model design parameters minimizing a specific misfit measure between the synthetic samples and the data. In order to avoid oversampling, a progressive batching strategy is employed, when an appropriate number of samples is estimated at each iteration and is adaptively updated using a specific test; see [17, 15, 61, 79, 11]. Such efficient stochastic programming methods are important for large-scale decision-making problems, especially in engineering design, where oversampling is significantly costly. The implementation also benefits from algorithmic differentiation for learning the model parameters. Once the surrogate model is calibrated, we use it to generate synthetic samples and to quantify the uncertainties in the elasto-plastic response of the lattice material. In particular, we estimate the expected values and the standard deviation of the effective tangent modulus for the lattice unit cell in different loading directions. Besides, perturbing the model parameters, we also study the effects of the imperfections on the effective Young's modulus.

The structure of the paper is as follows. In Section 2, we formulate the general problem and introduce notation. In Section 3, we introduce the surrogate material model and discuss several examples of the structure. In Section 4, we focus on a particular example, the octet-truss lattice, to demonstrate the process of calibration of the surrogate model and its application. First, we optimize the model parameters by fitting the CT data; the technical details of the optimization algorithm are given in Appendix A. Then, we use the calibrated model to generate synthetic samples and to quantify the uncertainties in the elasto-plastic response. In addition, we briefly discuss possible generalizations of the model in Section 5. Conclusion is given in Section 6.

2. Preliminaries

Let $\Omega = [0,1]^3$ be the 3-dimensional unit cube with periodic boundaries associated with a *representative volume element* (RVE) of the architected material. We consider a two-phase (binary) material, defined by the phase field

$$\varphi(\boldsymbol{x}) = \begin{cases} 0, & \text{if } \boldsymbol{x} \in \Omega_1, \\ 1, & \text{if } \boldsymbol{x} \in \Omega_2, \end{cases}$$

where the domain Ω_1 corresponds to the phase one and $\Omega_2 = \Omega \setminus \Omega_1$ to the phase two. Owing to uncertainties in the manufacturing process, the phase field φ is a random field. That is, for each $\boldsymbol{x} \in \Omega$, the value $\varphi(\boldsymbol{x})$ is a random value correlated with all other points in Ω. Thus, a digital 3D image representation of the phase field φ is given by a multivariate random vector.

We shall consider a series of particular realizations of the material distribution expressed by the phase field $\varphi(\boldsymbol{x};\omega)$, where ω is a sample indicator. For simplicity, we will also write $\varphi(\omega) := \varphi(\cdot;\omega)$. In particular, in our numerical experiments, we associate ω with the seed of a pseudo-random number generator. We also denote the mean value for any given functional f by $\mathbb{E}_\omega[f(\varphi(\omega))]$.

Let us further denote by φ_* the phase field characterizing the real manufactured material, which we will call the *target material*. In practice, this distribution is unknown, and only a small number of samples $X_i = \varphi_*(\omega_i)$, $i = 1 \dots N_{data}$, is accessible (e.g., as CT scans). Our purpose is to construct a surrogate mathematical model (a so-called *digital twin*) which allows the generation of synthetic samples with small computational cost and providing statistical properties similar to the target material φ_*.

Let us define a *surrogate material model* $\mathfrak{M}$ as a parametrized family of random phase fields $\varphi_\theta = \varphi(\theta)$, where θ is the vector of *design parameters*. Then, our digital twin is understood as a projection of φ_* onto the set $\mathfrak{M}$. That is, we want to find the *optimal* design parameters minimizing some distance measure between the distributions φ_θ and φ_*, formulated in terms of specific statistical descriptors. However, given only a set of samples of φ_*, we can minimize only the distance between the random field $\varphi(\theta)$ and the data set $\boldsymbol{X} = \{X_1, \dots\}$ of available realizations. In particular, we consider an objective function $\bar{J}(\theta) := \mathbb{E}_\omega[J(\varphi(\theta,\omega), \boldsymbol{X})]$, where $J(\varphi(\theta,\omega), \boldsymbol{X})$ denotes the distance from a particular surrogate sample ω to the data set $\boldsymbol{X}$. A choice of such a distance measure will be further discussed in detail in Section 4.1, where we formulate the corresponding stochastic optimization problem. A visual diagram of the calibration process of the surrogate material model is given in Figure 1.

In this way, extracting statistical information from the morphology of the given samples of the architected material, we construct a random field, which captures the principal geometric features and imitates the statistical properties of the target material samples. Then, employing a fast sampling procedure, we have access to an arbitrary number of synthetic samples that can be used for computational purposes, in particular, in Monte Carlo methods, for uncertainty quantification of the material response, quantities of interest, etc..

3. Surrogate material model

A common strategy to define a synthetic phase field is the *level-set method* (gray-scale thresholding), where the phases are defined as level-sets of some continuous *intensity field* (gray-scale); see [5, 6, 72, 4, 52, 34]. That is, we define the phase field as

$$\varphi(\boldsymbol{x};\theta,\omega) = \begin{cases} 0, & \text{if } u(\boldsymbol{x};\theta,\omega) < 0, \\ 1, & \text{otherwise}, \end{cases} \tag{1}$$

$\boldsymbol{x} \in \Omega$, where the random intensity field u is parametrized with θ, and ω is a sample indicator.

Our purpose is to construct the field which combines both a deterministic topological shape and uncertain imperfections. An example of such combination can be found, for example, in [34], where the intensity is considered as a Gaussian random field with the mean non-constant in Ω. In the current work, we consider a generalized *hybrid* model, where the intensity field is given by a linear combination of two intensities:

$$u(\boldsymbol{x};\theta,\omega) = (1-\alpha)\cdot u_1(\boldsymbol{x};\theta,\omega) + \alpha \cdot u_2(\boldsymbol{x};\theta,\omega), \qquad \alpha \in [0,1]. \tag{2}$$

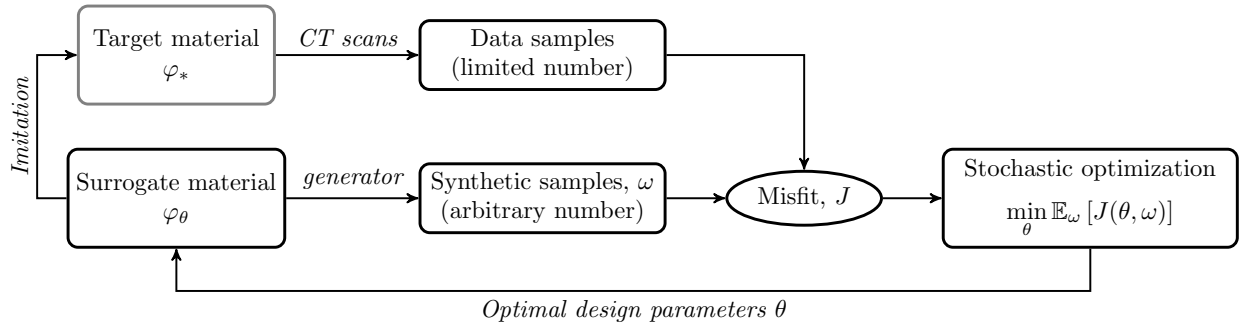

Figure 1: Visual scheme of the model calibration process. The target material distribution φ_* is unknown, however, a limited number of its samples (data) is given, e.g., as CT scans. In order to construct a surrogate which imitates the statistical properties of the target, we calibrate the design parameters θ of the surrogate model φ_θ minimizing the expectation of the misfit J between the synthetic samples (indexed by ω) and the data.

Here, u_1 defines the topological support, and u_2 is a random perturbation representing the imperfections. Note that the topological support u_1 can also exhibit uncertainties and that u_1 and u_2 are statistically independent. The parameter $\alpha \in [0; 1]$ defines the perturbation level, controlling the contribution of each term. In particular, $\alpha = 0$ corresponds to a structure without imperfections, and $\alpha = 1$ to an unstructured statistically homogeneous random media.

3.1. Perturbation field. Gaussian model

We define the intensity perturbation u_2 as a centered Gaussian random field with a given covariance function $\mathcal{C}(\boldsymbol{x}, \boldsymbol{y}) := \mathbb{E}[u_2(\boldsymbol{x})\, u_2(\boldsymbol{y})]$. As u_2 is already scaled with α in (2), we can assume, without loss of generality, that it has unit marginal variance $\mathcal{C}(\boldsymbol{x}, \boldsymbol{x}) = 1$ for all $\boldsymbol{x}$. Moreover, we assume that the random field u_2 is *statistically homogeneous* (stationary); that is, the covariance function is of the form $\mathcal{C}(\boldsymbol{x}, \boldsymbol{y}) = \mathcal{C}(\boldsymbol{x} - \boldsymbol{y})$.

A stationary Gaussian random field u_2 can be formally written as a convolution; see [54]:

$$u_2(\boldsymbol{x}) = \mathcal{C}_{\frac{1}{2}} * \eta(\boldsymbol{x}), \tag{3}$$

$\boldsymbol{x} \in \Omega$, where $*$ denotes the convolution product in $\mathbb{R}^3$, and η denotes the white Gaussian noise in $\mathbb{R}^3$ [26, 36]. The convolution kernel $\mathcal{C}_{\frac{1}{2}}$ is the *square root* of the the covariance operator in the sense that $\mathcal{C}_{\frac{1}{2}} * \mathcal{C}_{\frac{1}{2}} = \mathcal{C}$.

The covariance function defines how the values $u_2(\boldsymbol{x})$ are correlated at distinct points $\boldsymbol{x}$. We will consider herein a stationary covariance function of the form

$$\mathcal{C}(\boldsymbol{x} - \boldsymbol{y}) = \mathcal{M}_\nu \left(\frac{\sqrt{2\nu}}{\ell} \|\boldsymbol{x} - \boldsymbol{y}\| \right), \tag{4}$$

where $\|\cdot\|$ stands for the Euclidean norm, and $\mathcal{M}_\nu(x)$ is the normalized Matérn kernel [45, 66]:

$$\mathcal{M}_\nu(x) = \frac{x^\nu\, \mathcal{K}_\nu(x)}{2^{\nu-1}\Gamma(\nu)}.$$

Here, $\Gamma(x)$ and $\mathcal{K}_\nu(x)$ denote the Euler Gamma function and the modified Bessel function of the second kind [2, 73], respectively. The covariance function (4) is parametrized using two parameters: regularity $\nu > 0$ and correlation length $\ell > 0$, which thus are part of the design parameters vector of the surrogate model. The Matérn covariance is widely used in statistics [66, 25], geostatistics [47] and machine learning [76]. It represents a large class of covariance kernels, varying from the exponential ($\nu = 0.5$) to the squared-exponential ($\nu \to \infty$). In particular, the parameter ν controls the regularity of the function at zero: from weak singularity to infinite smoothness. The regularity of the kernel at the origin is directly related to the

smoothness of the level-set of the corresponding Gaussian field. However, because of the voxelized nature of the digital samples, the accuracy of the parameter ν is limited by the resolution of the image. Moreover, as shown in [34], when fitting the data to a Matérn model, there arises a manifold of *near-optimal* pairs (ν, ℓ); see also [18]. This makes the identification of a unique regularity ν and correlation length ℓ problematic.

The Gaussian model admits an efficient sampling procedure by use of the *spectral simulation method* employing the *Fast Fourier transform* (FFT) algorithm on a regular grid; see [38, 1] and the references therein. Indeed, by the convolution theorem, the convolution product in (3) reduces under Fourier transformation to a point-wise product of two fields:

$$\hat{u}(\boldsymbol{k}) = \hat{\mathcal{C}}_{\frac{1}{2}}(\boldsymbol{k})\, \hat{\eta}(\boldsymbol{k}),$$

where $\boldsymbol{k}$ corresponds to the wavevector, $\hat{u}$ and $\hat{\mathcal{C}}$ denote Fourier transforms of u and $\mathcal{C}$, respectively, and the Fourier transform $\hat{\eta}$ of the Gaussian noise is a complex Gaussian noise. The use of the FFT algorithm makes it possible to reduce the complexity of the generation of one sample from $\mathcal{O}(N^2)$ for the direct convolution approximation to $\mathcal{O}(N \log N)$, where N corresponds to the number of voxels. The Fourier transform in $\mathbb{R}^d$ of the Matérn kernel (4) is given explicitly by

$$\hat{\mathcal{C}}(\boldsymbol{k}) = |\hat{\mathcal{C}}_{\frac{1}{2}}(\boldsymbol{k})|^2 = \left(\frac{2\pi\ell^2}{\nu}\right)^{\frac{d}{2}} \frac{\Gamma(\nu + \frac{d}{2})}{\Gamma(\nu)} \left(1 + \frac{\ell^2}{2\nu} \|\boldsymbol{k}\|^2\right)^{-(\nu+\frac{d}{2})},$$

see [10, Vol.II, section 8.13, formula (3)].

Remark 1. A remarkable feature of a Matérn kernel is that it is associated with the Green's function for the fractional differential equation of the form (up to a factor)

$$\left(1 - \frac{\ell^2}{2\nu}\, \Delta\right)^{(\nu+\frac{d}{2})/2} u_2 = \eta,$$

where Δ is the Laplace operator; see [74, 75]. Thus, imposing boundary conditions and using variable coefficients, u_2 can be extended to a more general non-stationary random field, see, e.g., [60, 30, 41]. Though it is appropriate to mention these extension options, such models are beyond the scope of the current paper.

Example 1 (Gaussian level-set). Let $\alpha = 0.5$, and let the structure term u_1 in (2) be constant in Ω, i.e., $u_1(\boldsymbol{x}) \equiv \tau \in \mathbb{R}$ for $\boldsymbol{x} \in \Omega$. Then, the phase field φ is reduced to the threshold of a Gaussian random field with the mean τ and covariance $\mathcal{C}(\boldsymbol{x}, \boldsymbol{y})$, which corresponds to the common Gaussian level-set model; see, e.g., [70, 40, 35, 53, 80]. The resulting random field is statistically homogeneous and exhibits no particular topological shape.

In Figure 2, the sample (2a) presents a typical example of the Gaussian level-set model, while the samples (2b) and (2c) illustrate its modified variants. In particular, the sample (2b) is obtained by introducing the anisotropic metric in (4), i.e., considering the norm $\|\boldsymbol{A}_k(\omega)(\boldsymbol{x} - \boldsymbol{y})\|$ with the metric tensor $\boldsymbol{A}_k$ defined by a definite positive 3×3 matrix. Its eigenvalues control the lengthscales in the directions defined by the corresponding eigenvectors, which leads to an anisotropic phase field. The sample (2c) is obtained by replacing u_2 with $|u_2|$ (folded Gaussian distribution), which allows the connectivity properties of the two phases to be distinguished.

It is known that in the case of the Gaussian model, explicit closed-form formulas are available for statistical descriptors of the phase field φ, such as the mean (expected volume fraction) $\bar{\varphi}$ and the two-point correlation function; see, e.g., [37, 31]. In particular, the expected volume fraction $\bar{\varphi}$ is uniquely defined by the mean of the Gaussian intensity τ. However, in the general case, explicit formulas for statistical moments are generally not available, and thus the statistics must be approximated numerically using, e.g., Monte Carlo methods.

Though stationary random fields are easy to sample, they cannot reproduce the topological features of the statistically inhomogeneous media, such as randomly oriented particles or beams, cracks, imperfect lattice, etc.

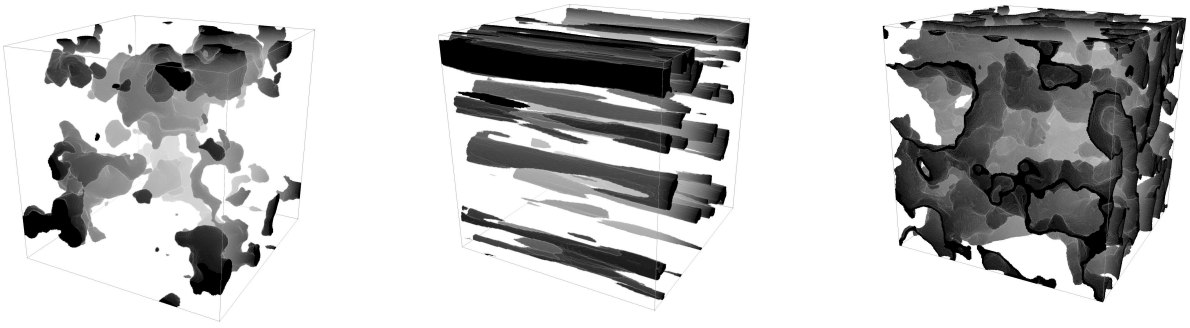

(a) $\bar{\varphi} = 0.1$, $\nu = 2$, $\ell = 0.1$

(b) $\bar{\varphi} = 0.1$, $\nu = 2$, $\ell = 0.05$, lengthscales $[10, 1, 1]$

(c) $\bar{\varphi} = 0.1$, $\nu = 2$, $\ell = 0.1$, folded Gaussian intensity

Figure 2: Examples of Gaussian level-set model (Example 1): (a) isotropic two-phase media; (b) anisotropic metric; (c) considering folded Gaussian distribution makes possible the distinction of connectivity of the phases.

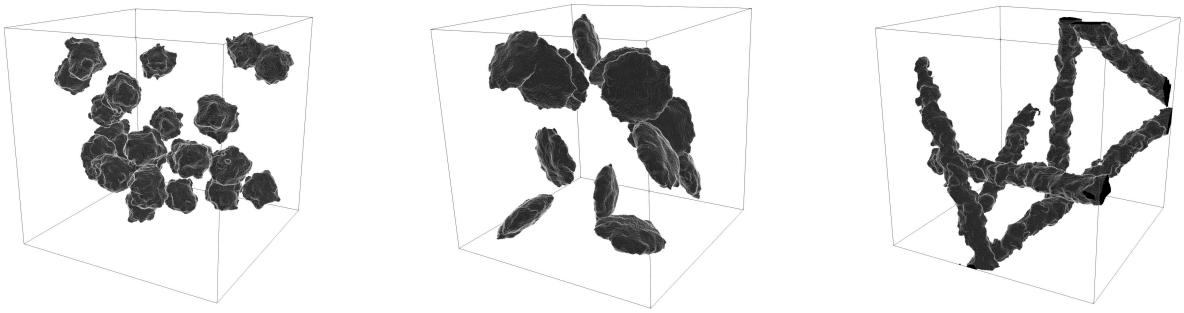

(a) isotropic with $\tau = 0.08$

(b) lengthscales $[3, 1, 3]$ with $\tau = 0.05$

(c) lengthscales $[200, 1, 1]$ with $\tau = 0.05$

Figure 3: Examples of the hybrid model with a collection of random points as support structure (see Example 2): (a) isotropic metric (spherical particles); (b) anisotropic metric (disks); (c) anisotropic metric (beams). The surface imperfections are of level $\alpha = 0.01$ with covariance of regularity $\nu = 2$ and correlation length $\ell = 0.03$.

(a) Synthetic cracks network (Example 3)

(b) Imperfect gyroid structure (Example 4)

Figure 4: (a) Example of a network of synthetic cracks (Example 3) with the mean opening $2\tau = 0.02$ and imperfections of level $\alpha = 0.005$ with covariance of regularity $\nu = 2$ and correlation length $\ell = 0.03$. (b) Example of a synthetic gyroid structure (Example 4) subject to surface imperfections of level $\alpha = 0.03$ with covariance of regularity $\nu = 2$ and correlation length $\ell = 0.015$, $\tau = 0.05$.

3.2. Topological support intensity

A very simple surrogate for a porous media can be obtained as a collection of particles of ideal shape, e.g., ellipsoids [69, 81]. Each such particle can be represented as level set of a cone in higher dimension [44]. This inspires us to introduce the intensity field for an arbitrary geometrical structure in (2) as a generalized cone given by the formula

$$u_1(\boldsymbol{x};\omega) = \tau - \rho(\boldsymbol{x}, \mathcal{G}(\omega)), \tag{5}$$

where $\rho(\boldsymbol{x}, \mathcal{G})$ denotes the distance from the point $\boldsymbol{x} \in \Omega$ to a manifold $\mathcal{G}$, which defines the geometrical structure; the parameter τ corresponds to the characteristic size of the structure and plays the role of the threshold in the level set model (1). Thus, the phase field (1) with intensity (5) and $\alpha = 0$, takes the value one in the points having a distance of at most τ from the manifold $\mathcal{G}$.

Example 2 (Collection of particles). An obvious example of structured material is a heterogeneous material with disjoint inclusions represented by collection of imperfect particles. Such structures can be constructed using the hybrid model (1)-(2) where the structure intensity u_1 is given by the so-called *maximum cones* [44] – the maximum of the set of cones centered in randomly distributed points. Thus, it can be written in the form (5) with the associated support structure given by a collection of randomly distributed points, particles centers, $\mathcal{G}(\omega) = \mathcal{G}_{\text{particles}}(\omega) = \{\boldsymbol{c}_k(\omega), \quad k = 1, \dots, N(\omega)\}$. Then, the distance to the manifold $\mathcal{G}_{\text{particles}}$ is given by the maximum of the distances to each of the centers:

$$\rho(\boldsymbol{x}, \mathcal{G}_{\text{particles}}(\omega)) = \min_{k \le N(\omega)} \|\boldsymbol{A}_k(\omega)(\boldsymbol{x} - \boldsymbol{c}_k(\omega))\|_p.$$

The particle shapes are defined by metric tensors $\boldsymbol{A}_k(\omega)$ and the norm type $\|\cdot\|_p$. In particular, the values $p = 1$, $p = 2$ or $p = \infty$ correspond to the diamond, ellipsoid or rectangular shapes, respectively. For each particle $k = 1, \dots, N$, the eigenvectors and eigenvalues of the metric tensor $\boldsymbol{A}_k$ define the principal axes (particle orientation) and the corresponding lengthscales, respectively.

Figure 3 shows examples of imperfect inclusions with different eigenlengths. The particle orientation is random and obtained from three uniformly distributed Euler angles.

Example 3 (Cracks). A networks of cracks in the solids can also be represented in this framework. The structure support is the boundary of a Voronoi tessellation, $\mathcal{G}(\omega) = \mathcal{G}_{\text{Voronoi}}(\omega)$, associated with the set of random points $\mathcal{G}_{\text{particles}}(\omega) = \{\boldsymbol{c}_k(\omega), \quad k = 1, \dots, N(\omega)\}$ from the previous example. In particular, we define the distance from a point $\boldsymbol{x} \in \Omega$ to the manifold $\mathcal{G}_{\text{Voronoi}}$ by

$$\rho(\boldsymbol{x}, \mathcal{G}_{\text{Voronoi}}(\omega)) = \frac{1}{2} \left| \frac{a^2(\boldsymbol{x}) - b^2(\boldsymbol{x})}{c(\boldsymbol{x})} \right|,$$

where a and b are the distances from $\boldsymbol{x}$ to the two closest centers k_1 and k_2, i.e., two minimum distances of $\{\rho(\boldsymbol{x}, \boldsymbol{c}_k) = \|\boldsymbol{x} - \boldsymbol{c}_k\|, \quad k = 1, \dots, N\}$; and c is the distance between $\boldsymbol{c}_{k_1}$ and $\boldsymbol{c}_{k_2}$. An example of a surrogate solid with cracks is given in Figure 4a. Note that in this case, the parameter τ in (5) corresponds to half of the mean crack opening size.

Example 4 (Gyroid). As another example, we consider a *gyroid* lattice [62], which is a popular architecture pattern in additive manufacturing. Although a gyroid is defined by the equations involving elliptical integrals [21], its close approximation is given by the level surface of a simple trigonometric expression [77]. Thus, this level-set function naturally defines our distance from a point $\boldsymbol{x} \in \Omega$ to the manifold $\mathcal{G}_{\text{gyroid}}$:

$$\rho(\boldsymbol{x}, \mathcal{G}_{\text{gyroid}}) = [\sin(2\pi x)\cos(2\pi y) + \sin(2\pi y)\cos(2\pi z) + \sin(2\pi z)\cos(2\pi x)]^2,$$

where $\boldsymbol{x} = (x, y, z) \in \Omega$. Note that without loss of generality, the square can be replaced with the absolute value. The parameter τ in (5) controls the thickness of the structure. An example of a surrogate gyroid structure is given in Figure 4b.

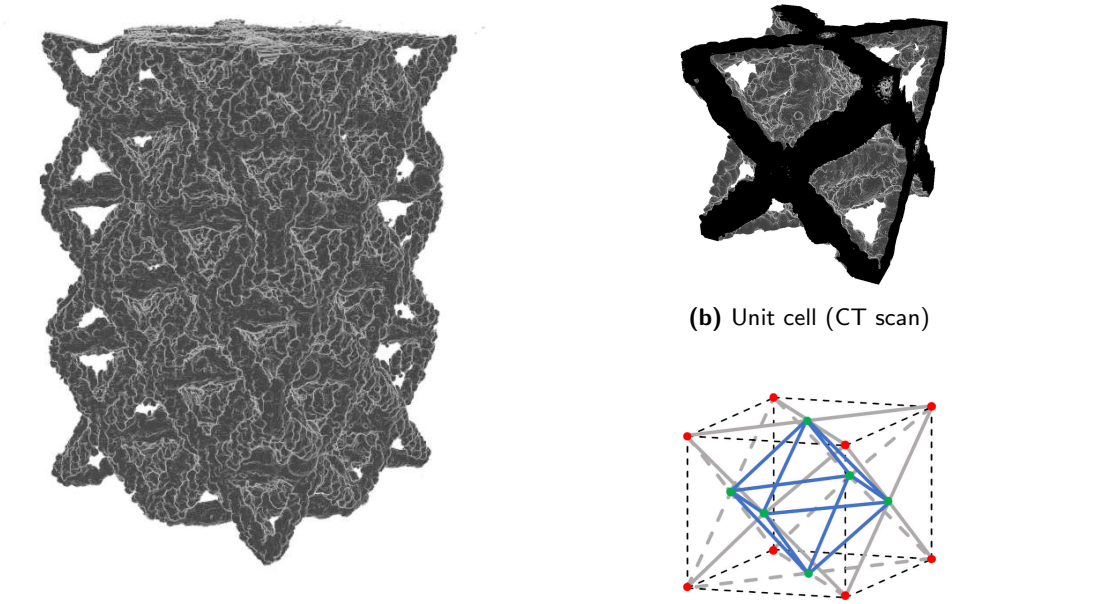

(a) Octet-truss lattice structure (CT scan)

(b) Unit cell (CT scan)

(c) Cell connectivity

Figure 5: Octet-truss lattice; see Example 5. (a): Computed Tomography (CT) of a lattice structure, (b): CT of a unit cell, (c): scheme of the truss connectivity in the unit cell.

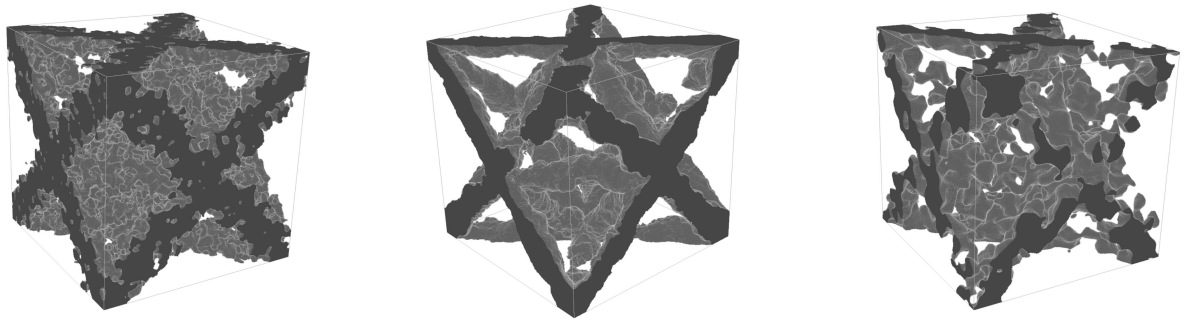

Figure 6: Examples of the surrogate octet lattice cell with surface imperfections (Example 5) using different values for the imperfection level α and the correlation length ℓ.

Example 5 (Octet-truss lattice). The octet-truss lattice structure (Figure 5) is another popular architecture pattern in additive manufacturing. The connectivity of the struts in its unit cell is schematically depicted in Figure 5c. Owing to the cell symmetry, it is sufficient to construct a quarter (subcell) of the cell. The nodes of the subcell are given in local coordinates by

$$\{\boldsymbol{p}_k,\ k = 1, \dots, 4\} = \{(0,0,0), (0,1,1), (1,0,1), (1,1,0)\}.$$

Then, the manifold $\mathcal{G}_{lattice}$ for the subcell is given by the set of the edges (struts):

$$\{e_k = (\boldsymbol{e}_{k,1}, \boldsymbol{e}_{k,2}),\ k = 1, \dots, 6\} = \{(\boldsymbol{p}_1, \boldsymbol{p}_2), (\boldsymbol{p}_1, \boldsymbol{p}_3), (\boldsymbol{p}_1, \boldsymbol{p}_4), (\boldsymbol{p}_2, \boldsymbol{p}_3), (\boldsymbol{p}_2, \boldsymbol{p}_4), (\boldsymbol{p}_3, \boldsymbol{p}_4)\}.$$

And, therefore, the distance to $\mathcal{G}_{lattice}$ is defined as

$$\rho(\boldsymbol{x}, \mathcal{G}_{\text{lattice}}) = \min_{k \leq 6} \rho(\boldsymbol{x}, e_k),$$

where $\rho(\boldsymbol{x}, e_k)$ is the distance from $\boldsymbol{x}$ to the line e_k which is given by the formula

$$\rho(\boldsymbol{x}, e_k) := \left[\frac{a^2 + b^2}{2} - \frac{c^2}{4} - \left(\frac{a^2 - b^2}{2\,c} \right)^2 \right]^{\frac{1}{2}},$$

and $a = \rho(\boldsymbol{x}, \boldsymbol{e}_{k,1})$, $b = \rho(\boldsymbol{x}, \boldsymbol{e}_{k,2})$, $c = \rho(\boldsymbol{e}_{k,1}, \boldsymbol{e}_{k,2})$ are Euclidean distances between the points.

Figure 6 shows examples of the surrogate octet lattice cell with different values of the uncertainty level α and the correlation length ℓ. The average strut radius is defined by the parameter τ in (5). Notice that with a high imperfection level α, the struts may even lose their connectivity, which is an important case in risk-adverseness problems and in failure probability analysis.

4. Application example: Octet-truss lattice

In this section, we demonstrate the calibration of a surrogate material model. To do this, we solve an optimization problem for finding the optimal design parameters of the model, minimizing the misfit between the synthetic model and the target material using a set of statistical/geometrical descriptors. Then, we proceed with an application of the surrogate material in stochastic homogenization. We use the calibrated model to generate an arbitrary number of synthetic samples within a Monte Carlo simulation for uncertainty quantification of the material effective properties.

In what follows, for our numerical experiments, we focus on a particular structure: octet-truss lattice cell (see Example 5). Owing to the manufacturing process, the resulting structure is perturbed by imperfections (see, e.g., Figure 7) that strongly affects the properties of the manufactured material and produce uncertainties in the material behavior. In particular, the difference in the effective properties of "as-designed" (defect-free) and "as-manufactured" (in the presence of imperfections) octet-truss lattices has been studied in [43, 32].

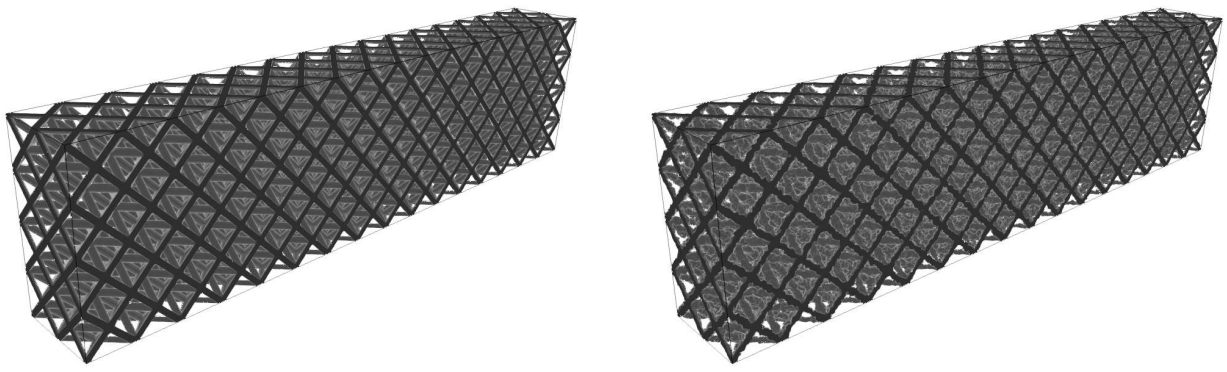

(a) **(b)**

Figure 7: Example of the octet-truss lattice structure (generated using the surrogate model): (a) "as-designed", (b) "as-manufactured".

4.1. Calibration of the model parameters

We consider the following stochastic optimization problem:

$$\min_{\theta} \mathbb{E}_{\omega} \left[J(\theta, \omega) \right], \tag{6}$$

where by J we denote a distance measure between a surrogate sample ω and the data. In order to define such a measure, we use a set of *geometrical descriptors* $\{d_i\}$. The explicit choice of descriptors will be discussed below. Then, we define J as misfits between the corresponding descriptors:

$$J(\theta, \omega) = \frac{1}{2} \sum_i \frac{\|d_i(\varphi_\theta(\omega)) - d_i^*\|^2}{\|d_i^*\|^2},$$

where d_i^* are the target descriptors obtained from the data, and the norm is the $\mathrm{L}^2(\Omega)$-norm.

The design parameters include here the average strut radius $\tau > 0$, the imperfection level $\alpha \in [0, 1]$ and the correlation length $\ell > 0$ of the surface imperfections. In order to avoid constrained optimization, we define the vector of design parameters as follows:

$$\theta := \{\log 2\tau, \operatorname{atanh}(2\alpha - 1), \log \ell\}. \tag{7}$$

Remark 2. Note that in (1), the Heaviside unit step function is not differentiable. Thus, in the optimization process, we replace it with its smooth approximation:

$$\varphi(\boldsymbol{x}; \omega) = \sigma(u(\boldsymbol{x}; \omega)) \tag{8}$$

with a smooth activation function approximating the unit step, e.g., $\sigma(x) = (1 + \tanh(x/\epsilon))/2$, where ϵ is small. In particular, we use $\epsilon = h^2$, where h stands for the voxel size.

Let us now discuss the choice of the descriptors $\{d_i\}$. We use the material volume fraction and its specific surface area as the two first geometrical descriptors. Specific surface area is the ratio of the surface area of the phase interface to the volume of the phase. For the regularized version of the two-phase material (8), we approximate the indicator function of the phase boundary with the absolute value of the gradient of the phase field. We will refer to it as the interface field $|\nabla\varphi(\boldsymbol{x})|$. These descriptors are global and cannot capture the local structure of the sample. To do this, we use the autocorrelation of the phase-field as another descriptor. For a statistically homogeneous random field, the field autocorrelation approximates the two-point correlation function [71]. Here, though the perturbation field is considered to be homogeneous, the octet cell structure is not. Moreover, the structure size dominates the perturbation correlation length scale. That is, the autocorrelation can provide information on the structure size, but it barely detects the localized properties of the perturbation. In order to get information on the perturbation, we need to consider the geometric features of the material surface. To this end, we use the autocorrelation of the interface field as the fourth descriptor. Thus, in our numerical experiments, we use the following geometrical descriptor of a sampled phase field φ:

$$\begin{aligned}
d_1(\varphi) &= \int_\Omega \varphi(\boldsymbol{x}) \, \mathrm{d}\boldsymbol{x}, \\
d_2(\varphi) &= \int_\Omega |\nabla\varphi(\boldsymbol{x})| \, \mathrm{d}\boldsymbol{x}, \\
d_3(\varphi; \boldsymbol{r}) &= \int_\Omega [\varphi(\boldsymbol{x} + \boldsymbol{r}) - d_1(\varphi)] \cdot [\varphi(\boldsymbol{x}) - d_1(\varphi)] \, \mathrm{d}\boldsymbol{x}, \\
d_4(\varphi; \boldsymbol{r}) &= \int_\Omega [|\nabla\varphi(\boldsymbol{x} + \boldsymbol{r})| - d_2(\varphi)] \cdot [|\nabla\varphi(\boldsymbol{x})| - d_2(\varphi)] \, \mathrm{d}\boldsymbol{x},
\end{aligned}$$

with the spatial lag $\boldsymbol{r} \in \Omega$. Given an image of the real sample $X = \varphi_*(\omega)$, the target descriptors are defined as $d_i^* := d_i(X)$. In case of a batch of the target material samples $\boldsymbol{X} = \{X_j = \varphi_*(\omega_j), \quad j = 1, \ldots, N_{data}\}$, the target descriptors can be defined as the average $d_i^* := \frac{1}{|\boldsymbol{X}|} \sum_{X \in \boldsymbol{X}} d_i(X)$.

4.2. Calibration results

We calibrate the model design parameters by solving the stochastic optimization problem (6). In order to avoid oversampling, a progressive batching strategy is applied, when the appropriate number of samples (*batch size* $|S_k|$) is estimated at each iteration k and is adaptively updated satisfying specific conditions; see [17, 15, 61, 79]. In our implementation, we follow the progressive batching LBFGS algorithm proposed in [16]. Technical details of the algorithm can be found in Appendix A.

The surrogate model generator is implemented using PyTorch [56], allowing to benefit from algorithmic differentiation for learning the model parameters. In particular, we use PyTorch-LBFGS package [63] for implementation of the progressive batching minimization.

The target material is the octet-truss lattice structure manufactured using an SLM printer [3] from 316L stainless steel; see Figure 5a. The relative density of the structure is 0.3. The images of the octet lattice have been obtained on the as-printed specimens at the In Situ Innovative Set-ups for X-ray micro-tomography on the ISIS4D platform [39]. Reconstruction of the tomographic data is performed with a filtered back-projection algorithm [29] using X-Act software. Similar X-ray tomography reconstructions have been used for exploring plasticity and fatigue phenomena on various materials, see, e.g., [27, 28, 64].

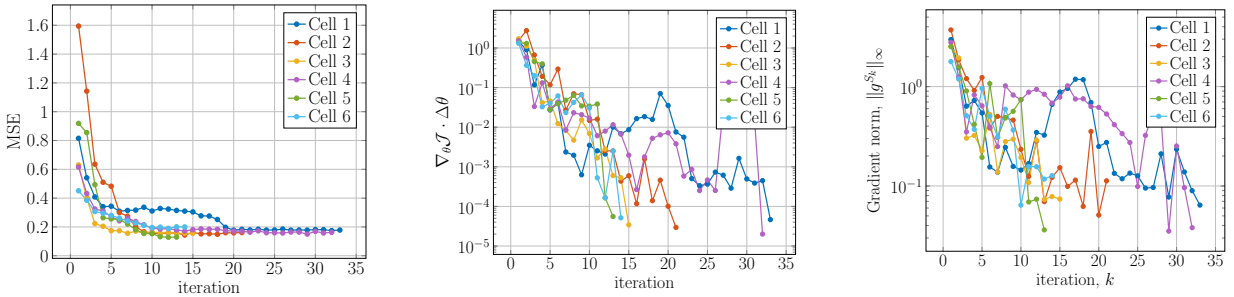

(a) Loss **(b)** Increment **(c)** Gradient norm

Figure 8: Convergence of the loss function (a), the loss increment (b) and the gradient norm (c) for each individual cell fitting.

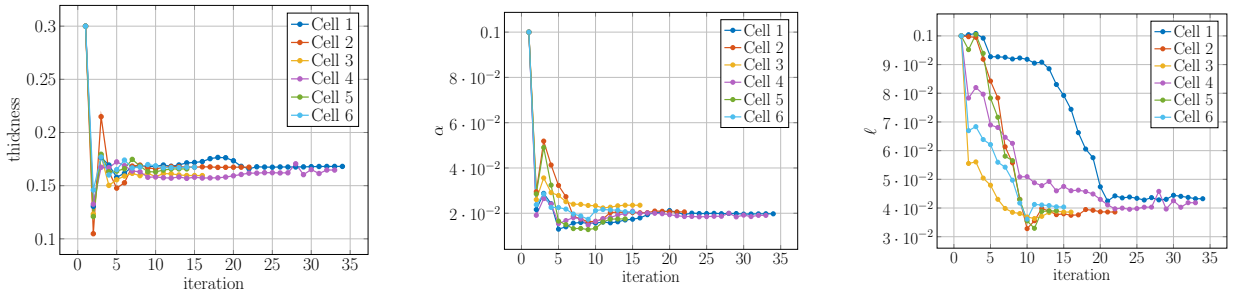

(a) Strut thickness **(b)** Imperfection level **(c)** Correlation length

Figure 9: Convergence of the model parameters for each individual cell fitting: (a) strut thickness 2τ; (b) imperfection level α; (c) correlation length ℓ.

We use six different lattice cells obtained from the CT image and fit the surrogate model individually on each of these targets, comparing at the end the results of these different fittings. We fix $\nu = 2$ assuming moderate smoothness of the imperfect interface. Therefore, our three parameters to calibrate are the strut thickness 2τ, the imperfection level α and the correlation length ℓ. The initial guess for the model parameters: $2\tau_0 = 0.3$, $\alpha_0 = 0.1$, $\ell_0 = 0.1$. The stopping criterion is reached when the loss increment is less than the

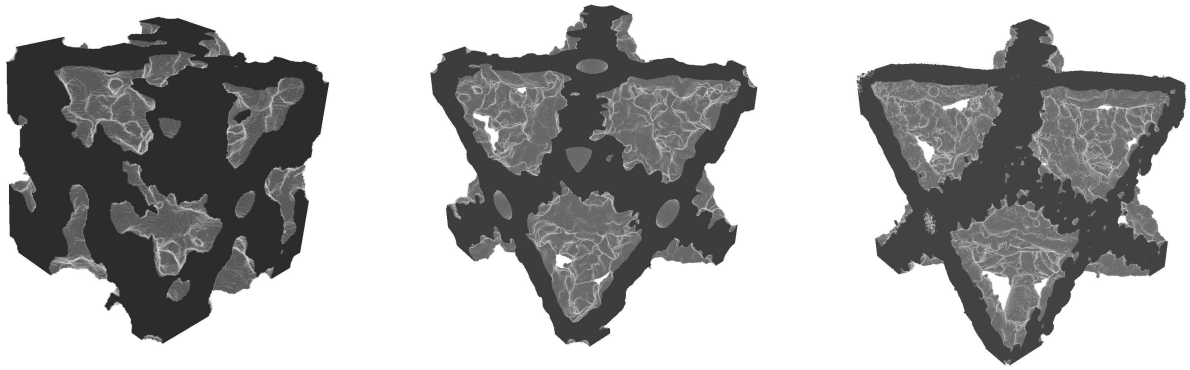

(a) Initial guess (sample), $2\tau = 0.3$, $\alpha = 0.1$, $\ell = 0.1$

(b) Calibration result (sample), $2\tau = 0.168$, $\alpha = 0.0198$, $\ell = 0.0432$

(c) Target (CT data – Cell 1)

Figure 10: Calibration of the surrogate model for the first cell: sample examples for the initial guess model (a), the resulting model (b) and the target cell (c).

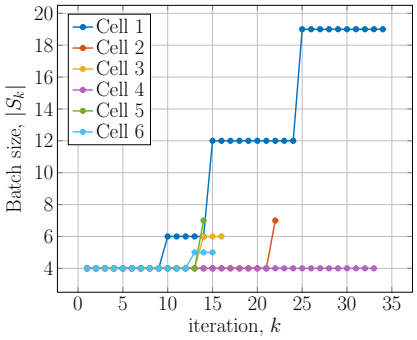

Figure 11: Progress of the batch size for each individual cell fitting.

fixed tolerance, precisely, $\nabla_\theta \bar{J}^{S_k} \cdot \Delta\theta < 10^{-4}$. For the model calibration as well for all our further numerical experiments, the size of the surrogate model samples is fixed at $2^7 \times 2^7 \times 2^7$ voxels. Figure 8 shows the convergence of the loss function, its increment and the max-norm of its gradient. And Figure 9 shows the evolution of the model parameters. Comparison of a calibrated model sample with an initial guess sample as well as with the target (the first cell) can be found in Figure 10. The progress of the batch size $|S_k|$ is depicted in Figure 11 for each individual cell fitting. For all our samples the stopping criterion is reached within 35 iterations, but in some cases 15 iterations were sufficient. Although only one data sample was considered for each case, we can observe that the deviation of the resulting parameters is small; see (9) below. This is due to the fact that the distribution of the imperfections over the material surface is statistically homogeneous, and even one sample provides enough information on the statistical properties of the uncertainties. Note that in the general case, the required number of data samples can be larger depending on the deviation of the resulting design parameters. In case more data samples are available, Bayesian inference techniques can also be employed.

4.3. Uncertainty quantification of elasto-plastic response

Owing to the structure imperfection, the material properties, such as effective bulk and shear moduli, computed on one material sample are random variables. Once the surrogate material model is calibrated with

respect to the real material data, we can proceed with uncertainty quantification of the material properties and, in particular, estimation of their probability distribution. To this end, using synthetic samples, we employ a crude Monte Carlo method to approximate the expected value and the standard deviation of the *quantities of interest* (QoIs).

In our application, the quantity of interest is the effective tangent modulus of the lattice material. Let the base material of the lattice be assumed elasto-plastic with isotropic linear hardening, Young's modulus 200 GPa, Poisson ratio 0.3, yield stress 0.4 GPa and the hardening modulus 0.6 GPa. To compute the elasto-plastic material response, we use the software CraFT [13] – a mesh-free solver using a Fast-Fourier Transform algorithm and based on the Suquet-Moulinec method [67, 49, 50, 46], in particular, using the Monchiet-Bonnet scheme [48]. The contrast of the Young's moduli of the phases is fixed at 10^{-4}.

Let $\boldsymbol{n}$ be a loading direction, $\|\boldsymbol{n}\| = 1$. We impose in 25 uniform loading steps (loading time $t \in [0, 1]$) the macroscopic stress $\boldsymbol{\sigma}$ in the direction $\boldsymbol{n}$ (uniaxial extension) resulting in 1% macroscopic deformation in the direction $\boldsymbol{n}$. That is, $\boldsymbol{n}^T\boldsymbol{\varepsilon}\boldsymbol{n} = 0.01$ at $t = 1$, where $\boldsymbol{\varepsilon}$ denotes the resulting macro strain. We consider 10 different directions of $\boldsymbol{n}$ from the regular grid (4 nodes per axis) in the triangle defined by the points $(1, 0, 0)$, $(1, 1, 0)$ and $(1, 1, 1)$. All the other directions can be obtained by symmetry of the octet-truss lattice cell.

For each loading direction $\boldsymbol{n}$, we compute the elasto-plastic material responses of 20 material samples, generated using the surrogate material model calibrated in Section 4.2. In particular, we assume the design parameters (7), $\theta = \{\log 2\tau, \operatorname{atanh}(2\alpha-1), \log \ell\}$, to be random i.i.d. normally distributed with the mean and the standard deviation estimated using the calibration results for different cells from Section 4.2, precisely,

$$\theta = \begin{bmatrix} \log 2\tau \\ \operatorname{atanh}(2\alpha - 1) \\ \log \ell \end{bmatrix} \sim \mathcal{N}\left(\begin{bmatrix} -1.8 \\ -1.94 \\ -3.21 \end{bmatrix}, \begin{bmatrix} 0.018^2 & & \\ & 0.046^2 & \\ & & 0.043^2 \end{bmatrix} \right). \tag{9}$$

Thus, for each surrogate sample ω, we first sample the design parameters $\theta(\omega)$ and then the corresponding phase field realization $\varphi(\theta(\omega), \omega)$.

For each surrogate material sample, from the values $\varepsilon_{nn} := \boldsymbol{n}^T\boldsymbol{\varepsilon}\boldsymbol{n}$ and $\sigma_{nn} := \boldsymbol{n}^T\boldsymbol{\sigma}\boldsymbol{n}$, the corresponding tangent moduli $\frac{\partial\sigma_{nn}}{\partial\varepsilon_{nn}}$ are computed via finite differences. From the obtained dataset, we estimate the expected value and the standard deviation of the tangent modulus. Exploiting the symmetry properties of the structure, we illustrate in Figure 12 the directional variation of the tangent modulus $\frac{\partial\sigma_{nn}}{\partial\varepsilon_{nn}}$ for the surrogate model octet-lattice cell at different loading time t. There, the polar plots (a)-(b) correspond to the cell cross-sections (the planes A and B) shown in Figure 12c. Owing to the symmetry, all other cross-sections are equivalent to these two. The expected values of the tangent modulus are depicted with solid lines, while the transparent areas around represent the associated standard deviation. We also plot with dashed lines the modulus values corresponding to the as-designed (defect-free) structure, i.e., with the imperfection level $\alpha = 0$. A 3D plot of directional variation of the Young's modulus for the defect-free structure can be found in Figure 12d. In Figure 13, we plot the tangent modulus $\frac{\partial\sigma_{nn}}{\partial\varepsilon_{nn}}$ (expected value and deviation) in the directions co-linear to $(1, 0, 0)$, $(1, 1, 0)$ and $(1, 1, 1)$ as function of the applied deformation ε_{nn}. The scale of y-axis is logarithmic. We observe that the deviation magnitude changes with the strain proportionally to the expectation. The volume fraction of the defect-free structure ($\alpha = 0$) is 0.273; in the presence of imperfections, the expected value for the volume fraction is 0.282 with the standard deviation 0.009. Note that the tangent modulus near $t = 0$ corresponds to the Young's modulus and that the obtained values are in a good agreement with the numerical and experimental results, e.g., in [20, 57]. Besides, we observe that the plastic effects strongly depend on the loading direction; in particular, the most stiff direction varies with deformation. Note also that the structure with imperfections is always less stiff than the as-designed one; moreover, the effective yield stress of the as-designed cell is higher than in the presence of imperfections.

4.4. Analysis of imperfections effect

In this section, in order to assess the effect of the defects, we study the sensitivity of the Young's modulus to the model parameters describing the imperfections – the level α and the correlation length ℓ. To this end, for variable values of the parameters α and ℓ, we compute the Young's modulus in two directions: $(1, 0, 0)$ – a minimum stiffness direction, and $(1, 1, 1)$ – a maximum stiffness direction. The strut thickness is fixed to

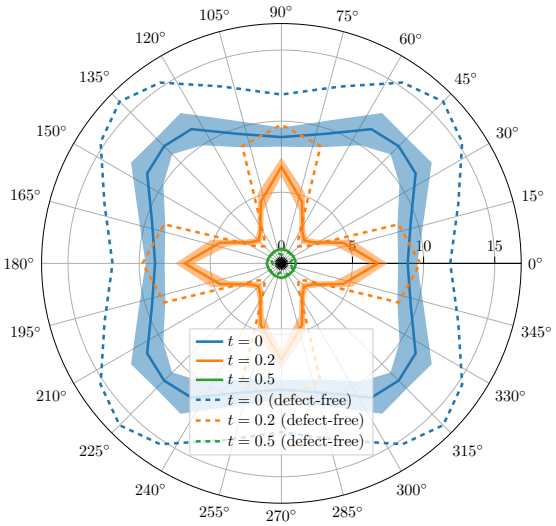

(a) Plane A

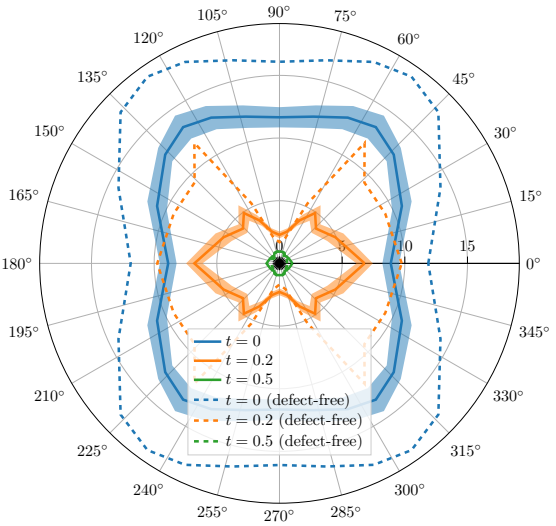

(b) Plane B

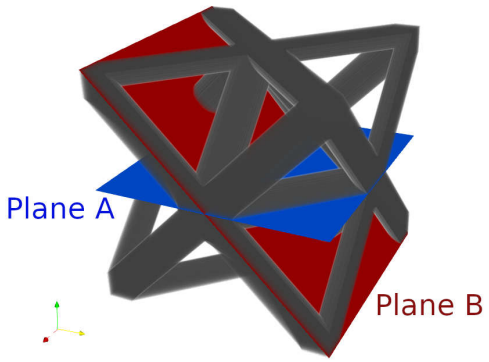

(c) Scheme of the cross-sections

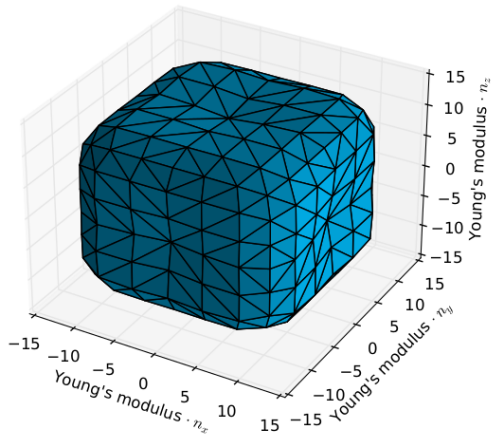

(d) Young's modulus of the defect-free structure

Figure 12: Directional variation of the tangent modulus at loading time $t = 0, 0.2, 0.5$: (a): in the plane A, (b): in the plane B. Solid line – expected value, transparent area – standard deviation, dashed line – defect-free case. (c): position of the planes A and B. Owing to the symmetry, all other cross-sections are equivalent to these two. (d): 3D plot of directional variation of the Young's modulus for the defect-free structure. We computed 10 different 3D directions (4 for each of cross-sections A and B) in the triangle defined by the points $(1, 0, 0)$, $(1, 1, 0)$ and $(1, 1, 1)$. All the other directions are obtained by symmetry of the octet-truss lattice cell.

$2\tau = 0.165$. We consider the model parameters values in the domain $[0, 0.03] \times [0.01, 0.1]$ of the (α, ℓ) plane (7×7 mesh grid). For each pair (α, ℓ), we estimate the expected value of Young's modulus computed using 20 surrogate material samples. The resulting moduli are depicted in the contour plots in Figure 14 (using linear interpolation), where the abscissa corresponds to α, and the ordinate – to ℓ. The left plot corresponds to the directional minimum of the Young's modulus, while the right one corresponds to the maximum. We observe that the Young's modulus decreases with increasing imperfections level. Besides, for high enough α, the correlation length starts to affect the Young's modulus which decreases with ℓ.

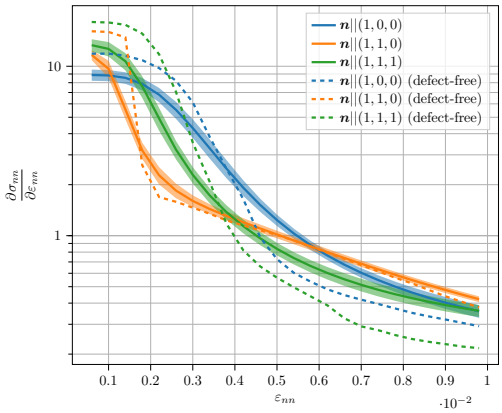

Figure 13: Tangent modulus in the directions co-linear to $(1,0,0)$, $(1,1,0)$ and $(1,1,1)$ as function of the strain ε_{nn}. Solid line – expected value, transparent area – standard deviation.

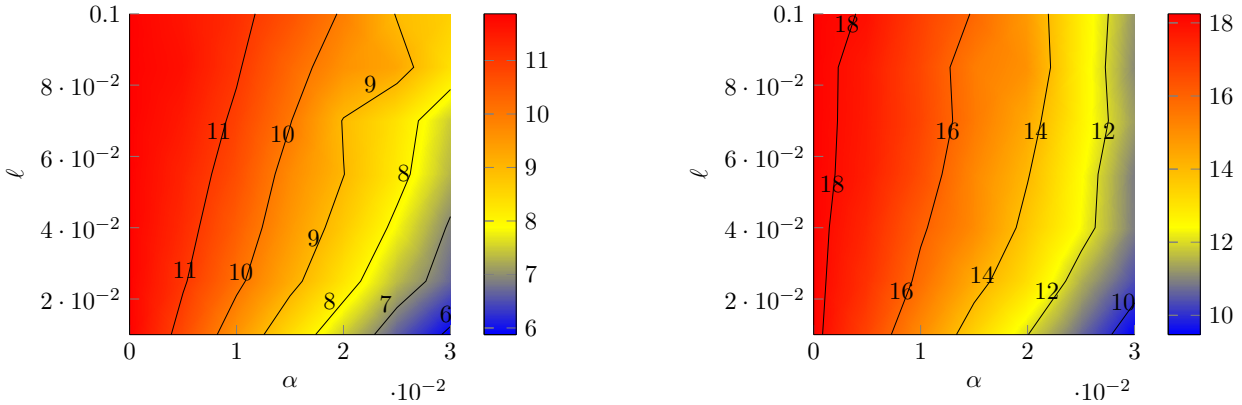

(a) Directional minimum of Young's modulus

(b) Directional maximum of Young's modulus

Figure 14: Contour plots of Young's modulus in (α, ℓ) plane illustrating the effects of imperfections of the octet-truss lattice cell; (a): directional minimum, (b): directional maximum.

5. Generalizations

In this section, in addition, we briefly comment on a couple of generalizations of the proposed surrogate model: application to risk-aversion and an extension to multi-phase materials.

5.1. Risk-aversion

The optimization algorithm can be used not only for calibration of a surrogate model, but also for material design, i.e., for construction of a surrogate material with desired mechanical properties. In this case, the expectations of the relevant quantities of interest can be used as the statistical descriptors. Moreover, in the context of material design there naturally arises the risk aversion problem, when it is more important to minimize the probability of extreme values (tail of the distribution) than the expectation. In many industrial applications, a common choice for such risk measures is the so-called *conditional value-at-risk* CVaR [58]:

$$\mathrm{CVaR}_\beta(\xi) := \mathbb{E}\left[\xi \,\middle|\, \xi > \mathrm{VaR}_\beta(\xi)\right],$$

where ξ is a random variable, and the *value-at-risk* $\mathrm{VaR}_\beta(\xi)$ is the β-quantile of ξ, $0 < \beta < 1$. For example, let the random variable ξ denote a stress measure of a structure (e.g., the maximum of von Mises

stress). When high values correspond to plastification or failure, lower values of ξ are preferable. The quantile $\mathrm{VaR}_\beta(\xi)$ represents the most optimistic state which can be achieved in the worst $(1-\beta)\cdot 100\%$ of possible events, while $\mathrm{CVaR}_\beta(\xi)$ represents the expected value of ξ in these events. It is known (see [59]) that CVaR can be written via a scalar minimization problem:

$$\mathrm{CVaR}_\beta(\xi) = \inf_{q\in\mathbb{R}} \mathbb{E}\left[q + \frac{1}{1-\beta}(\xi - q)_+\right],$$

where $(\,\cdot\,)_+ := \max(0,\cdot)$. Therefore, minimization of CVaR can be written in the form (6) with an additional parameter q, which converges to the β-quantile.

5.2. Multi-phase fields

As further extension of the discussed surrogate model, one can consider a multi-phase field:

$$\varphi(\boldsymbol{x}) = \arg\max \boldsymbol{W}\boldsymbol{u}(\boldsymbol{x}),$$

where $\boldsymbol{u} = \{u_1, \dots, u_n\}$ is a vector random field, and $\boldsymbol{W}$ is a matrix of weights, such that $\boldsymbol{W}\boldsymbol{u}$ is a vector of intensities corresponding to n different phases. The *argmax* activation returns the index of the most intense phase at the point. Its smooth approximation is based on the *softmax* function. We remark that for $n = 2$, $\boldsymbol{u} = \{u_1, u_2\}$ and $\boldsymbol{W}$ being diagonal with the entries $\alpha - 1$ and α, we recover the hybrid model (1)-(2). A study of this extended model is a possible direction for future work. Here, we only provide a 2D example in Figure 15 in order to outline the potential of this model in application to simulation of the morphologic and crystallographic textures of the polycrystalline grains in the additively manufactured materials [7, 8].

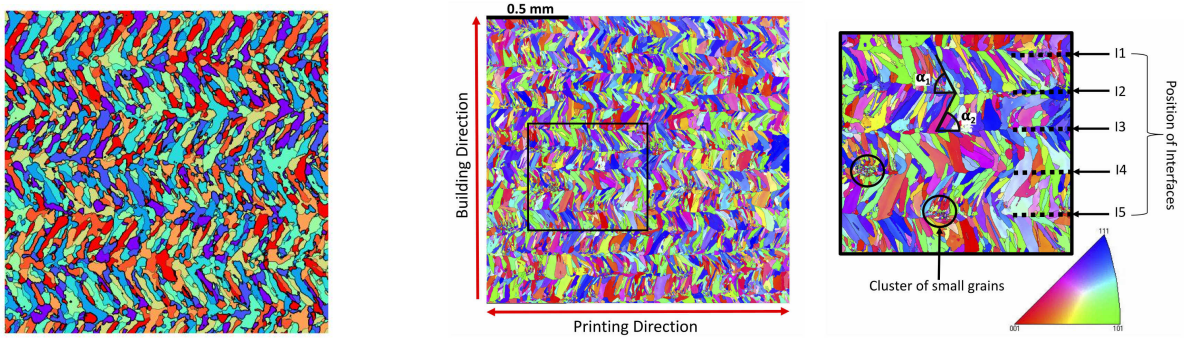

(a) Synthetic grain texture **(b)** Real grain texture

Figure 15: (a) Example of a synthetic multi-phase sample imitating polycrystalline grain texture in a manufactured material (not calibrated design parameters, 10 phases). (b) Electron Backscatter Diffraction of a specimen from bidirectionally-printed single-track thickness 316L stainless steel wall built by directed energy deposition (taken from [7]), and a zoom showing the interfaces between layers, cluster of small grains at interfaces and the morphological grain angles for both direction of printing.

6. Conclusion

We proposed a surrogate material model which combines the topological shape and random imperfections. Given in a unified form, the model is able to reproduce a variety of imperfect structures: porous media, fibers, cracks, lattice structures. We used an imperfect octet-truss lattice cell for an illustration of the surrogate model application. From a small amount of the real samples, we calibrated the model design parameters minimizing the misfit between the corresponding geometrical descriptors. The implementation can benefit from algorithmic differentiation and progressive batching techniques.

Using the calibrated surrogate model, we are able to generate synthetic material samples and to use them in Monte Carlo type methods for uncertainty quantification of the material response. We illustrated the applicability of the surrogate model in estimating the expectation and the deviation of the effective tangent modulus, as well as in investigating the sensitivity of the effective modulus to the imperfections. Note that more sophisticated estimators of the probability distributions of QoIs can also be considered. For example, by computing a number of statistical moments of QoIs, one can construct an approximation of the associated probability distribution function using a moment-matching method (such as the maximum entropy principle).

Note also that we used only geometrical descriptors obtained from the target material samples to calibrate the model and to use it consequently to sample the effective material properties. In the general case, the effective moduli themselves can be also used as descriptors. That is, in addition to the geometrical descriptors, one can use *mechanical descriptors*, such as effective material moduli, maximum stress, etc.. In this case, while the mechanical descriptors of the surrogate samples have to be computed numerically, the corresponding target descriptor d_i^* can be provided by experimental measurements.

Since the as-designed and as-manufactured materials have quite different effective properties, it is extremely important to take imperfections into account in the material design process. Thus, the surrogate material model proposed in this work is shown to be a promising approach for numerical analysis of the impact of imperfections in the manufactured materials.

Acknowledgments

UK and BW were supported by the German Research Foundation by grants WO671/11-1 and the European Union's Horizon 2020 research and innovation programme under grant agreement No 800898. AC and PLT were partly supported by the André Citroën Chair. We want to express our thanks to Jerome Hosdez and Nikolai Khailov for providing the image samples, and to Brendan Keith and Florian Beiser for helpful discussions on the optimization algorithm.

Appendix A. Sub-sampled quasi-Newton minimization

In this appendix, we present the details of the sub-sampled quasi-Newton minimization algorithm used for calibration of the surrogate model. The method is proposed in [16]. We also refer the interested reader to [14, 15, 61, 79].

Let us consider a minimization problem in the form

$$\min_{\theta} \bar{J}(\theta) = \mathbb{E}_{\omega}\left[J(\theta;\omega)\right].$$

We define each particular sample with a random seed $\omega \in \mathcal{S} = \mathbb{N} \cap [0, 10^3]$ of the pseudo random generator used to sample the uncertainties. The sub-sampled quasi-Newton method iteratively computes a sequence θ_k of approximations of the optimal vector of design parameters, using the update formula

$$\theta_{k+1} = \theta_k - \alpha_k H_k \bar{g}_k^{S_k},$$

where $\bar{g}_k^{S_k}$ is the batch (sub-sampled) gradient of $\bar{J}$:

$$\bar{g}_k^{S_k} := \frac{1}{|S_k|} \sum_{\omega \in S_k} g_k(\omega), \qquad g_k(\omega) := \nabla_\theta J(\theta_k;\omega),$$

with a set (batch) of material samples (random seeds) S_k of the size $|S_k|$. Above, H_k is a positive definite quasi-Newton operator – an approximation of the inverse Hessian matrix. Using the limited memory BFGS method [42], it is defined by the recursive formula

$$H_{k+1} = \left(\mathrm{Id} - \frac{\Delta\theta_k \, \Delta g_k^T}{\Delta\theta_k^T \Delta g_k}\right) H_k \left(\mathrm{Id} - \frac{\Delta\theta_k \, \Delta g_k^T}{\Delta\theta_k^T \Delta g_k}\right) + \frac{\Delta\theta_k \, \Delta\theta_k^T}{\Delta\theta_k^T \Delta g_k},$$

Algorithm 1: Sub-sampled L-BFGS

Result: Approximated optimal design parmaters θ_{opt}
Input: initial guess θ_0, initial sample size $|S_0|$

repeat
  Sample batch $S_k \subset \mathcal{S}$ of the size $|S_k|$;
  Compute the bound b_k by (A.1) ;
  if $|S_k| < b_k$ **then**
    Sample $\Delta S_k \subset \mathcal{S} \setminus S_k$ with $|\Delta S_k| = \lceil b_k \rceil - |S_k|$;
    Set $S_k = S_k \cup \Delta S_k$;
  end
  Compute $\bar{g}_k^{S_k}$;
  Compute $p_k = -H_k \bar{g}_k^{S_k}$ using two-loop recursion;
  Compute initial steplength α_k ;
  while *the Armijo condition* (A.2) *is not satisfied* **do**
    Set $\alpha_k = \alpha_k/2$;
  end
  Update $\theta_{k+1} = \theta_k + \alpha_k p_k$;
  Update the curvature pairs $(\Delta g_j, \Delta \theta_j)$;
  Set $|S_{k+1}| = |S_k|$;
  Increment k ;
until *convergence*;

with the curvature pair $\Delta g_k := \bar{g}_{k+1}^{S_k} - \bar{g}_k^{S_k}$ and $\Delta\theta_k := \theta_{k+1} - \theta_k$. A common approach to compute the operator H_k is given by the L-BFGS two-loop recursion algorithm [78].

The key idea of a progressive batching approach is that at each iteration, the sample size is selected such that it satisfies the inner-product quasi-Newton test [14]:

$$|S_k| \geq b_k := \frac{\mathrm{Var}_{\omega \in S_k}[(g_k(\omega))^T H_k^2 \bar{g}_k^{S_k}]}{\kappa^2 \| H_k \bar{g}_k^{S_k} \|^4}, \tag{A.1}$$

with some scalar parameter κ (we use $\kappa = 1$). Here, Var denotes the sampled variance of some random variable f_k, given by

$$\mathrm{Var}_{\omega \in S_k}[f_k(\omega)] := \frac{1}{|S_k| - 1} \sum_{\omega \in S_k} \| f_k(\omega) - \bar{f}_k^{S_k} \|^2.$$

Whenever condition (A.1) is not satisfied, the sample size $|S_k|$ is increased.

To find the steplength α_k, we perform a backtracking line search, satisfying the Armijo condition (see also [16]):

$$\bar{J}^{S_k}(\theta_k - \alpha_k H_k \bar{g}_k^{S_k}) \leq \bar{J}^{S_k}(\theta_k) - c_1 \alpha_k \, [\bar{g}_k^{S_k}]^T H_k \bar{g}_k^{S_k}, \tag{A.2}$$

where $\bar{J}^{S_k} := \frac{1}{|S_k|} \sum_{\omega \in S_k} J(\theta_k; \omega)$ and the constant $c_1 = 10^{-4}$. The initial steplength is $\alpha_k = \left(1 + \frac{\mathrm{Var}_{S_k}[\bar{g}_k]}{|S_k| \cdot \| \bar{g}_k^{S_k} \|}\right)^{-1}$. The full procedure is schematically outlined in Algorithm 1.

References

[1] Abrahamsen, P., Kvernelv, V., Barker, D., 2018. Simulation of Gaussian random fields using the Fast Fourier Transform (FFT), in: ECMOR XVI-16th European Conference on the Mathematics of Oil Recovery, European Association of Geoscientists & Engineers. pp. 1–14.

[2] Abramowitz, M., Stegun, I.A., 1965. Handbook of mathematical functions: with formulas, graphs, and mathematical tables. volume 55. Courier Corporation.

[3] AddUp Global Additive Solutions, FormUp 350 3D-printer. https://addupsolutions.com.
[4] Allaire, G., Dapogny, C., Delgado, G., Michailidis, G., 2014. Multi-phase structural optimization via a level set method. ESAIM: control, optimisation and calculus of variations 20, 576–611.
[5] Allaire, G., Jouve, F., Toader, A.M., 2002. A level-set method for shape optimization. Comptes Rendus Mathematique 334, 1125–1130.
[6] Allaire, G., Jouve, F., Toader, A.M., 2004. Structural optimization using sensitivity analysis and a level-set method. Journal of computational physics 194, 363–393.
[7] Balit, Y., Charkaluk, E., Constantinescu, A., 2020a. Digital image correlation for microstructural analysis of deformation pattern in additively manufactured 316l thin walls. Additive Manufacturing 31, 100862.
[8] Balit, Y., Guévenoux, C., Tanguy, A., Upadhyay, M.V., Charkaluk, E., Constantinescu, A., 2020b. High resolution digital image correlation for microstructural strain analysis of a stainless steel repaired by directed energy deposition. Materials Letters 270, 127632.
[9] Balit, Y., Margerit, P., Charkaluk, E., Constantinescu, A., 2021. Crushing of additively manufactured thin-walled metallic lattices: Two-scale strain localization analysis. Mechanics of Materials , 103915.
[10] Bateman, H., 1954. Tables of integral transforms. McGraw-Hill, N.Y.
[11] Beiser, F., Keith, B., Urbainczyk, S., Wohlmuth, B., 2020. Adaptive sampling strategies for risk-averse stochastic optimization with constraints. arXiv preprint arXiv:2012.03844 .
[12] Bessa, M., Bostanabad, R., Liu, Z., Hu, A., Apley, D.W., Brinson, C., Chen, W., Liu, W.K., 2017. A framework for data-driven analysis of materials under uncertainty: Countering the curse of dimensionality. Computer Methods in Applied Mechanics and Engineering 320, 633–667.
[13] Boittin, G., Labé, A., Moulinec, H., Silva, F., Suquet, P., . CraFT ("Composite response and Fourier Transforms"). https://lma-software-craft.cnrs.fr.
[14] Bollapragada, R., Byrd, R., Nocedal, J., 2018a. Adaptive sampling strategies for stochastic optimization. SIAM Journal on Optimization 28, 3312–3343.
[15] Bollapragada, R., Byrd, R.H., Nocedal, J., 2019. Exact and inexact subsampled newton methods for optimization. IMA Journal of Numerical Analysis 39, 545–578.
[16] Bollapragada, R., Nocedal, J., Mudigere, D., Shi, H.J., Tang, P.T.P., 2018b. A progressive batching l-bfgs method for machine learning, in: International Conference on Machine Learning, PMLR. pp. 620–629.
[17] Byrd, R.H., Chin, G.M., Nocedal, J., Wu, Y., 2012. Sample size selection in optimization methods for machine learning. Mathematical programming 134, 127–155.
[18] De Oliveira, V., 2000. Bayesian prediction of clipped gaussian random fields. Computational Statistics & Data Analysis 34, 299–314.
[19] DebRoy, T., Mukherjee, T., Wei, H., Elmer, J., Milewski, J., 2021. Metallurgy, mechanistic models and machine learning in metal printing. Nature Reviews Materials 6, 48–68.
[20] Deshpande, V.S., Fleck, N.A., Ashby, M.F., 2001. Effective properties of the octet-truss lattice material. Journal of the Mechanics and Physics of Solids 49, 1747–1769.
[21] Gandy, P.J., Klinowski, J., 2000. Exact computation of the triply periodic g (gyroid') minimal surface. Chemical Physics Letters 321, 363–371.
[22] Garland, A.P., White, B.C., Jared, B.H., Heiden, M., Donahue, E., Boyce, B.L., 2020. Deep convolutional neural networks as a rapid screening tool for complex additively manufactured structures. Additive Manufacturing 35, 101217.
[23] Gavazzoni, M., Foletti, S., Pasini, D., 2022. Cyclic response of 3d printed metamaterials with soft cellular architecture: The interplay between as-built defects, material and geometric non-linearity. Journal of the Mechanics and Physics of Solids 158, 104688.
[24] Gayon-Lombardo, A., Mosser, L., Brandon, N.P., Cooper, S.J., 2020. Pores for thought: generative adversarial networks for stochastic reconstruction of 3D multi-phase electrode microstructures with periodic boundaries. npj Computational Materials 6, 1–11.
[25] Gneiting, T., Guttorp, P., 2012. Studies in the history of probability and statistics XLIX On the Matern correlation family. Biometrika 93, 989–995.
[26] Hida, T., Kuo, H.H., Potthoff, J., Streit, L., 2013. White noise: an infinite dimensional calculus. volume 253. Springer Science & Business Media.
[27] Hosdez, J., Langlois, M., Witz, J., Limodin, N., Najjar, D., Charkaluk, E., Osmond, P., Forre, A., Szmytka, F., 2019. Plastic zone evolution during fatigue crack growth: Digital image correlation coupled with finite elements method. International Journal of Solids and Structures 171, 92–102.
[28] Hosdez, J., Limodin, N., Najjar, D., Witz, J., Charkaluk, E., Osmond, P., Forré, A., Szmytka, F., 2020. Fatigue crack growth in compacted and spheroidal graphite cast irons. International Journal of Fatigue 131, 105319.
[29] Kak, A.C., Slaney, M., 2001. Principles of computerized tomographic imaging. SIAM.
[30] Keith, B., Khristenko, U., Wohlmuth, B., 2021. A fractional pde model for turbulent velocity fields near solid walls. Journal of Fluid Mechanics 916.
[31] Khristenko, U., Constantinescu, A., Le Tallec, P., Oden, J.T., Wohlmuth, B., 2019. A statistical framework for generating microstructures of two-phase random materials: application to fatigue analysis. arXiv preprint arXiv:1907.02412 .
[32] Korshunova, N., Alaimo, G., Hosseini, S., Carraturo, M., Reali, A., Niiranen, J., Auricchio, F., Rank, E., Kollmannsberger, S., 2021a. Bending behavior of octet-truss lattice structures: Modelling options, numerical characterization and experimental validation. Materials & Design 205, 109693.
[33] Korshunova, N., Alaimo, G., Hosseini, S.B., Carraturo, M., Reali, A., Niiranen, J., Auricchio, F., Rank, E., Kollmannsberger, S., 2021b. Image-based numerical characterization and experimental validation of tensile behavior of octet-truss

lattice structures. Additive Manufacturing , 101949.
[34] Korshunova, N., Papaioannou, I., Kollmannsberger, S., Straub, D., Rank, E., 2021c. Uncertainty quantification of microstructure variability and mechanical behaviour of additively manufactured lattice structures. arXiv preprint arXiv:2103.09550 .
[35] Koutsourelakis, P.S., Deodatis, G., 2006. Simulation of multidimensional binary random fields with application to modeling of two-phase random media. Journal of engineering mechanics 132, 619–631.
[36] Kuo, H.H., 2018. White noise distribution theory. CRC press.
[37] Lantuéjoul, C., 2001. Geostatistical simulation: models and algorithms. 1139, Springer Science & Business Media.
[38] Le Ravalec, M., Noetinger, B., Hu, L.Y., 2000. The FFT moving average (FFT-MA) generator: An efficient numerical method for generating and conditioning Gaussian simulations. Mathematical Geology 32, 701–723.
[39] Limodin, N., Rougelot, T., Hauss, G., 2013. Isis4d-in situ innovative set-ups under x-ray microtomography. `http://isis4d.univ-lille1.fr`.
[40] Lin, P.S., Clayton, M.K., 2005. Properties of binary data generated from a truncated gaussian random field. Communications in Statistics—Theory and Methods 34, 537–544.
[41] Lindgren, F., Bolin, D., Rue, H., 2021. The spde approach for gaussian and non-gaussian fields: 10 years and still running. `arXiv:2111.01084`.
[42] Liu, D.C., Nocedal, J., 1989. On the limited memory bfgs method for large scale optimization. Mathematical programming 45, 503–528.
[43] Liu, L., Kamm, P., Garcia-Moreno, F., Banhart, J., Pasini, D., 2017. Elastic and failure response of imperfect three-dimensional metallic lattices: the role of geometric defects induced by selective laser melting. Journal of the Mechanics and Physics of Solids 107, 160–184.
[44] Mantz, H., Jacobs, K., Mecke, K., 2008. Utilizing Minkowski functionals for image analysis: a marching square algorithm. Journal of Statistical Mechanics: Theory and Experiment 2008, P12015.
[45] Matérn, B., 1986. Spatial Variation. volume 36 of *Lecture Notes in Statistics*. Springer New York, New York, NY.
[46] Michel, J., Moulinec, H., Suquet, P., 2001. A computational scheme for linear and non-linear composites with arbitrary phase contrast. International Journal for Numerical Methods in Engineering 52, 139–160.
[47] Minasny, B., McBratney, A.B., 2005. The Matérn function as a general model for soil variograms. Geoderma 128, 192–207.
[48] Monchiet, V., Bonnet, G., 2012. A polarization-based fft iterative scheme for computing the effective properties of elastic composites with arbitrary contrast. International Journal for Numerical Methods in Engineering 89, 1419–1436.
[49] Moulinec, H., Suquet, P., 1994. A fast numerical method for computing the linear and nonlinear mechanical properties of composites. Comptes rendus de l'Académie des sciences. Série II. Mécanique, physique, chimie, astronomie. .
[50] Moulinec, H., Suquet, P., 1998. A numerical method for computing the overall response of nonlinear composites with complex microstructure. Computer methods in applied mechanics and engineering 157, 69–94.
[51] Moussa, A., Melancon, D., El Elmi, A., Pasini, D., 2021. Topology optimization of imperfect lattice materials built with process-induced defects via powder bed fusion. Additive Manufacturing 37, 101608.
[52] Nika, G., Constantinescu, A., 2019. Design of multi-layer materials using inverse homogenization and a level set method. Computer Methods in Applied Mechanics and Engineering 346, 388–409.
[53] Ogorodnikov, V.A., Kablukova, E.G., Prigarin, S.M., 2018. Stochastic models of atmospheric clouds structure. Statistical Papers 59, 1521–1532.
[54] Oliver, D.S., 1995. Moving averages for gaussian simulation in two and three dimensions. Mathematical Geology 27, 939–960.
[55] Pasini, D., Guest, J.K., 2019. Imperfect architected materials: Mechanics and topology optimization. MRS Bulletin 44, 766–772.
[56] Paszke, A., Gross, S., Massa, F., Lerer, A., Bradbury, J., Chanan, G., Killeen, T., Lin, Z., Gimelshein, N., Antiga, L., Desmaison, A., Kopf, A., Yang, E., DeVito, Z., Raison, M., Tejani, A., Chilamkurthy, S., Steiner, B., Fang, L., Bai, J., Chintala, S., 2019. PyTorch: An Imperative Style, High-Performance Deep Learning Library, in: Wallach, H., Larochelle, H., Beygelzimer, A., d'Alché-Buc, F., Fox, E., Garnett, R. (Eds.), Advances in Neural Information Processing Systems 32. Curran Associates, Inc., pp. 8024–8035.
[57] Qi, D., Yu, H., Liu, M., Huang, H., Xu, S., Xia, Y., Qian, G., Wu, W., 2019. Mechanical behaviors of SLM additive manufactured octet-truss and truncated-octahedron lattice structures with uniform and taper beams. International Journal of Mechanical Sciences 163, 105091.
[58] Rockafellar, R.T., Royset, J.O., 2015. Engineering decisions under risk averseness. ASCE-ASME Journal of Risk and Uncertainty in Engineering Systems, Part A: Civil Engineering 1, 04015003.
[59] Rockafellar, R.T., Uryasev, S., et al., 2000. Optimization of conditional value-at-risk. Journal of risk 2, 21–42.
[60] Roininen, L., Huttunen, J.M., Lasanen, S., 2014. Whittle-Matérn priors for Bayesian statistical inversion with applications in electrical impedance tomography. Inverse Probl. Imaging 8, 561–586.
[61] Roosta-Khorasani, F., Mahoney, M.W., 2019. Sub-sampled newton methods. Mathematical Programming 174, 293–326.
[62] Schoen, A.H., 1970. Infinite periodic minimal surfaces without self-intersections. National Aeronautics and Space Administration.
[63] Shi, H.J.M., Mudigere, D., . PyTorch-LBFGS. `https://github.com/hjmshi/PyTorch-LBFGS`.
[64] Shi, H.L., Hosdez, J., Rougelot, T., Xie, S.Y., Shao, J.F., Talandier, J., 2021. Analysis of local creep strain field and cracking process in claystone by x-ray micro-tomography and digital volume correlation. Rock Mechanics and Rock Engineering 54, 1937–1952.
[65] Snow, Z., Nassar, A., Reutzel, E.W., 2020. Review of the formation and impact of flaws in powder bed fusion additive manufacturing. Additive Manufacturing , 101457.

[66] Stein, M.L., 2012. Interpolation of spatial data: some theory for kriging. Springer Science & Business Media.
[67] Suquet, P., 1990. A simplified method for the prediction of homogenized elastic properties of composites with a periodic structure. Comptes Rendus De L Academie Des Sciences Serie II 311, 769–774.
[68] Tancogne-Dejean, T., Mohr, D., 2018. Elastically-isotropic truss lattice materials of reduced plastic anisotropy. International Journal of Solids and Structures 138, 24–39.
[69] Tarantino, M., Zerhouni, O., Danas, K., 2019. Random 3d-printed isotropic composites with high volume fraction of pore-like polydisperse inclusions and near-optimal elastic stiffness. Acta Materialia 175, 331–340.
[70] Teubner, M., 1991. Level surfaces of Gaussian random fields and microemulsions. EPL (Europhysics Letters) 14, 403.
[71] Torquato, S., 2013. Random heterogeneous materials: microstructure and macroscopic properties. volume 16. Springer Science & Business Media.
[72] Wang, M.Y., Wang, X., 2004. "color" level sets: a multi-phase method for structural topology optimization with multiple materials. Computer Methods in Applied Mechanics and Engineering 193, 469–496.
[73] Watson, G.N., 1995. A treatise on the theory of Bessel functions. Cambridge University press, Cambridge.
[74] Whittle, P., 1954. On stationary processes in the plane. Biometrika , 434–449.
[75] Whittle, P., 1963. Stochastic-processes in several dimensions. Bulletin of the International Statistical Institute 40, 974–994.
[76] Williams, C.K., Rasmussen, C.E., 2006. Gaussian processes for machine learning. the MIT Press 2, 4.
[77] Wohlgemuth, M., Yufa, N., Hoffman, J., Thomas, E.L., 2001. Triply periodic bicontinuous cubic microdomain morphologies by symmetries. Macromolecules 34, 6083–6089.
[78] Wright, S., Nocedal, J., 1999. Numerical optimization. Springer Science 35, 7.
[79] Xie, Y., Bollapragada, R., Byrd, R., Nocedal, J., 2020. Constrained and composite optimization via adaptive sampling methods. arXiv preprint arXiv:2012.15411 .
[80] Zerhouni, O., Brisard, S., Danas, K., 2021. Quantifying the effect of two-point correlations on the effective elasticity of specific classes of random porous materials with and without connectivity. International Journal of Engineering Science 166, 103520.
[81] Zerhouni, O., Tarantino, M., Danas, K., 2019. Numerically-aided 3d printed random isotropic porous materials approaching the hashin-shtrikman bounds. Composites Part B: Engineering 156, 344–354.